







Anisotropy of the magnetic and transport properties of EuZn_2As_2

Zhi-Cheng Wang ^{1,*}, Emily Been ^{2,3,*}, Jonathan Gaudet^{4,5}, Gadeer Matook A. Alqasseri^{6,7}, Kyle Fruhling ¹, Xiaohan Yao ¹, Uwe Stuhr ⁸, Qinqing Zhu^{9,10}, Zhi Ren^{9,10}, Yi Cui¹¹, Chunjing Jia², Brian Moritz², Sugata Chowdhury^{6,7}, Thomas Devereaux^{2,11} and Fazel Tafti ^{1,†}

¹*Department of Physics, Boston College, Chestnut Hill, Massachusetts 02467, USA*

²*Stanford Institute for Materials and Energy Sciences, SLAC National Accelerator Laboratory, 2575 Sand Hill Road, Menlo Park, California 94025, USA*

³*Department of Physics, Stanford University, Stanford, California 94305, USA*

⁴*NIST Center for Neutron Research, National Institute of Standards and Technology, Gaithersburg, Maryland 20899, USA*

⁵*Department of Materials Science and Eng., University of Maryland, College Park, Maryland 20742-2115, USA*

⁶*Department of Physics and Astrophysics, Howard University, Washington, DC 20059, USA*

⁷*IBM-Howard Quantum Center, Howard University, Washington, DC 20059, USA*

⁸*Laboratory for Neutron Scattering and Imaging, Paul Scherrer Institut, 5232 Villigen-PSI, Switzerland*

⁹*School of Science, Westlake University, 18 Shilongshan Road, Hangzhou 310024, People's Republic of China*

¹⁰*Institute of Natural Sciences, Westlake Institute for Advanced Study, 18 Shilongshan Road, Hangzhou 310024, People's Republic of China*

¹¹*Department of Materials Science and Engineering, Stanford University, Stanford, California 94305, USA*



(Received 20 February 2022; accepted 30 March 2022; published 14 April 2022)

Several recent studies have shown that the anisotropy in the magnetic structure of EuCd_2As_2 plays a significant role in stabilizing the Weyl nodes. To investigate the relationship between magnetic anisotropy and Weyl physics, we present a comparative study between EuZn_2As_2 and EuCd_2As_2 that are isostructural but with different magnetic anisotropy. We performed structural analysis, electronic transport, and magnetization experiments on millimeter-sized single crystals of EuZn_2As_2 , and compared the results to those of EuCd_2As_2 . By combining the first principle calculations and neutron diffraction experiment, we identify the magnetic ground state of EuZn_2As_2 as A-type antiferromagnetic order with a transition temperature ($T_N = 19.6$ K) twice that of EuCd_2As_2 . Like EuCd_2As_2 , the negative magnetoresistance of EuZn_2As_2 is observed after suppressing the resistivity peak at T_N with increasing fields. However, the anisotropy in both transport and magnetization are much reduced in EuZn_2As_2 . The difference could be ascribed to the weaker spin-orbit coupling, more localized d orbitals, and a larger contribution from the Eu s orbitals in the zinc compound, as suggested by the electronic band calculations. The same band structure effect could be also responsible for the observation of a smaller nonlinear anomalous Hall effect in EuZn_2As_2 compared to EuCd_2As_2 .

DOI: [10.1103/PhysRevB.105.165122](https://doi.org/10.1103/PhysRevB.105.165122)

I. INTRODUCTION

Recent observations of anisotropic magnetoresistance, spin-fluctuation-induced Dirac nodes, and nonlinear anomalous Hall effect in EuCd_2As_2 have made this material an interesting candidate to study the interplay between topology and magnetism [1–8]. EuCd_2As_2 undergoes an A-type antiferromagnetic (AFM) order at 9.2 K with considerable anisotropy between the in-plane and out-of-plane magnetic susceptibilities [7]. Its resistivity shows a peak near the Néel temperature (T_N) which is suppressed in an external magnetic field, and thus may be related to the fluctuations of the AFM order [9–15]. Its Hall resistivity also shows a peak that is nonlinear in either the magnetic field or magnetization, hence the name nonlinear anomalous Hall effect (NLAHE) [2]. To bring the resistivity peak and NLAHE to higher temperatures,

it is necessary to increase the temperature scale of the AFM order and its fluctuations. Here we present EuZn_2As_2 as an analog of EuCd_2As_2 but with a T_N twice as high, possibly due to the weaker spin-orbit coupling (SOC) and more localized d orbitals in the zinc compound. We show that (a) both the resistivity peak and NLAHE are shifted to higher temperatures in EuZn_2As_2 compared to EuCd_2As_2 , and (b) the anisotropy in both transport and magnetization are reduced in the zinc compound. We present a comprehensive study of the crystal structure, magnetic susceptibility, heat capacity, anomalous Hall effect of EuZn_2As_2 and EuCd_2As_2 , and theoretical electronic structure to understand the factors that control the anisotropy of physical properties and their temperature scales in these materials.

II. METHODS

(a) *Crystal growth.* Single crystals of EuZn_2As_2 were grown in Sn flux, by using sublimed ingots of europium (99.9%), zinc powder (99.9%), arsenic powder (99.99%), and

*These authors contributed equally to this work.

†fazel.tafti@bc.edu

TABLE I. Crystallographic data and Rietveld refinement parameters for EuZn_2As_2 and EuCd_2As_2 in the space group $P\bar{3}m1$. The Wyckoff sites are Eu $1a$ (0,0,0), Zn/Cd $2d$ ($1/3, 1/3, z$), and As $2d$ ($1/3, 2/3, z$) with full occupancy.

Material	EuZn_2As_2	EuCd_2As_2
Lattice parameters		
a (Å)	4.21118(3)	4.44016(4)
c (Å)	7.18114(6)	7.32779(9)
V (Å ³)	110.2888(24)	125.1125(38)
c/a	1.705	1.650
Z	1	1
Coordinates (z)		
Zn/Cd	0.62859(16)	0.63342(21)
As	0.26743(16)	0.24593(29)
Debye-Waller factors B_{iso}		
Eu (Å ²)	1.183(28)	1.820(90)
Zn/Cd (Å ²)	1.738(43)	1.813(86)
As (Å ²)	1.163(32)	1.840(83)
R factors		
R_p	6.95	8.22
R_{exp}	6.25	6.59
χ^2	2.25	2.47
Bond distances (Å)		
Eu-As ($\times 6$)	3.0983(8)	3.1336(13)
As-Zn/Cd ($\times 3$)	2.5434(5)	2.7117(9)
As-Zn/Cd ($\times 1$)	2.5935(17)	2.8395(3)
Bond angles (°)		
As-Zn/Cd-As	111.76(4)	109.91(6)

tin shots (99.999%) as the starting materials. The elements were mixed in a mole ratio $\text{Eu}:\text{Zn}:\text{As}:\text{Sn} = 1:1:1:8$. The excess of Eu prohibits the formation of Zn_3As_2 impurity. The mixture was loaded into an alumina crucible inside an evacuated quartz ampule and slowly heated to 1100 °C, held for 24 h, cooled to 900 °C at 3 °C/h, cooled to 600 °C at 5 °C/h, and finally centrifuged to remove the flux. The crystals grow as millimeter-sized hexagonal prisms with metallic luster, and are stable in air.

(b) *Powder x-ray diffraction.* A few crystals were ground for the powder x-ray diffraction using a Bruker D8 ECO instrument equipped with 40 keV copper source and a 1D LYNXEYE XE detector. The FullProf suite was used for the structural refinements [16].

(c) *Resistivity, heat capacity, and magnetization measurements.* Transport data were collected with a standard four-probe technique using a Quantum Design Physical Property Measurement System (PPMS) Dynacool with a high-resolution rotator option. The heat capacity data were measured using the PPMS with a relaxation time method. Crystals with clear facets were selected to measure DC magnetization using a Quantum Design Magnetic Property Measurement System (MPMS-3).

(d) *Neutron diffraction.* A single crystal of EuZn_2As_2 was mounted on an Al plate with the \bar{b} axis vertical to the scattering plane so the Bragg scattering within the ($h0l$) plane could be probed. The experiment was performed with the thermal neutron triple-axis spectrometer EIGER at the SINQ spallation neutron source at the Paul Scherrer Institute (PSI). The energy of the incident neutrons was 14.7 meV with a resolution of ~ 0.66 meV. A fully open collimation configuration

was used to maximize the neutron flux as well as PG filters to eliminate high-order Bragg reflections. Representational analysis of magnetism was performed using SARAh [17].

(e) *First-principles calculations.* The total energies and band structures were calculated using the projector-augmented wave (PAW) version [18] of density functional theory (DFT) with the Perdew-Burke-Ernzerhof (PBE) exchange correlation functional [19], as implemented in Vienna *ab initio* simulation package (VASP) [20–23]. The pseudopo-

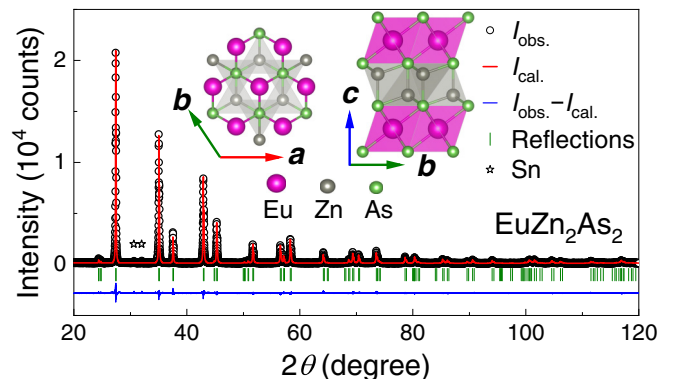


FIG. 1. Powder x-ray diffraction of EuZn_2As_2 (black circles), Rietveld refinement in space group $P\bar{3}m1$ (red lines), fit residual curve (blue lines), and hkl indices (green ticks) are shown. The black stars show Bragg peaks from the Sn flux. Inset shows the crystal structure viewed from [001] and [100] directions. The Eu, Zn, and As atoms are shown as magenta, green, and gray balls, respectively. The structural refinement of EuCd_2As_2 is presented in Fig. S1 of the SM [26].

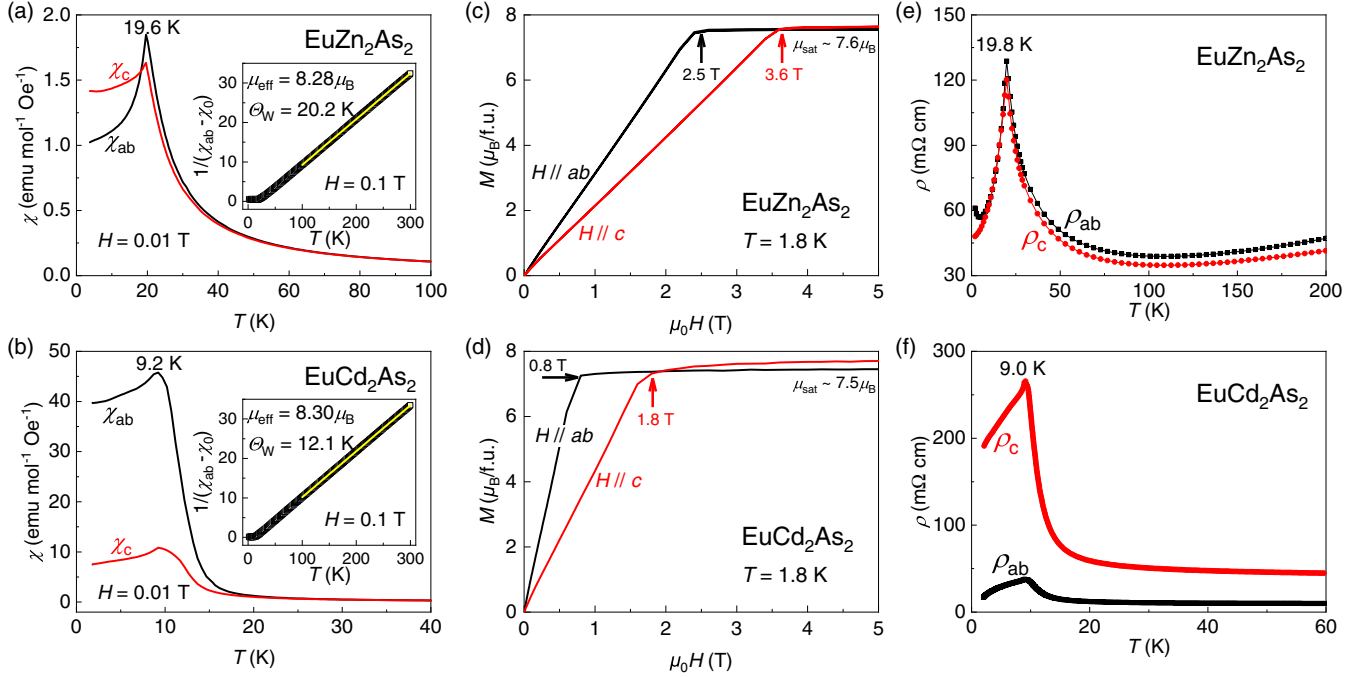


FIG. 2. Temperature dependence of anisotropic magnetic susceptibility with in-plane (χ_{ab}) and out-of-plane fields (χ_c) are plotted for (a) EuZn_2As_2 and (b) EuCd_2As_2 . The insets show the Curie-Weiss analysis. Magnetization curves as a function of both in-plane (black) and out-of-plane (red) fields are plotted for (c) EuZn_2As_2 and (d) EuCd_2As_2 . Temperature dependence of resistivity is plotted with in-plane (black) and out-of-plane (red) current for (e) EuZn_2As_2 and (f) EuCd_2As_2 . Data in panel (f) is from Ref. [1]. More information is provided in Fig. S2 within the SM [26].

tential for Eu had $4f$ electrons explicitly in the valence, therefore we added a Hubbard $U = 5$ eV and spin-orbit coupling (SOC) to correctly describe their localization [6,24]. These GGA+ U +SOC calculations were performed using the rotationally invariant method by Dudarev *et al.* [25]. The self-consistent field (SCF) calculations used a k -point Monkhorst-Pack grid of $8 \times 16 \times 16$ for the 2-Eu supercell, $8 \times 16 \times 8$ for the 4-Eu supercell, $16 \times 16 \times 4$ for 3-Eu supercell, and $5 \times 5 \times 9$ for the 9-Eu supercell (see Supplemental Material [SM] [26]).

III. RESULTS AND DISCUSSIONS

A. Structural analysis

The powder x-ray diffraction pattern of EuZn_2As_2 in Fig. 1 is refined in the trigonal space group $P\bar{3}m1$ (#164). The structural parameters are listed in Table I and compared to those of the sister compound EuCd_2As_2 . Inset of Fig. 1 shows that the structure comprises alternating layers of edge-sharing ZnAs_4 tetrahedra and edge-sharing EuAs_6 octahedra. Table I shows that all bond lengths are slightly shorter and bond angles are slightly wider in the Zn compound. Despite subtle changes of crystal structure between EuZn_2As_2 and EuCd_2As_2 , we will show in Sec. III G that the electronic structure changes visibly and leads to changes of electronic and magnetic anisotropy between the two compounds.

B. Magnetic and Transport Anisotropy

EuZn_2As_2 and EuCd_2As_2 order at $T_N = 19.6$ K and 9.2 K, respectively. The magnetic transition is marked by a peak in

the susceptibility data under both in-plane and out-of-plane fields [χ_{ab} and χ_c in Figs. 2(a) and 2(b)]. The transition is considered antiferromagnetic (AFM) based on (i) absence of splitting between the zero-field-cooled (ZFC) and field-cooled (FC) susceptibility data (Fig. S2 within SM [26]) and (ii) absence of hysteresis in $M(H)$ curves [Figs. 2(c) and 2(d)]. The Curie-Weiss fits in the insets of Figs. 2(a) and 2(b) show effective moments of approximately $8.3 \mu_B$ in both compounds, slightly larger than the theoretical value of $8 \mu_B$ for Eu^{2+} . The saturated moments at high fields in Figs. 2(c) and 2(d) are also slightly larger than the theoretical value of $7 \mu_B$ for Eu^{2+} . Both observations are due to a known effect, namely the polarization of d orbitals induced by the large f moments in either Eu^{2+} or Gd^{3+} with $4f^7$ configuration [27,28].

The Curie-Weiss fits (insets of Figs. 2(a) and 2(b) and Fig. S3 within SM [26]) yield positive Weiss temperatures ($\Theta_W > 0$) indicative of ferromagnetic (FM) correlations in both compounds. The presence of FM correlations despite AFM ordering implies either A-type AFM (interlayer AFM and intralayer FM coupling) or C-type AFM order (interlayer FM and intralayer AFM coupling). Recent resonant elastic x-ray scattering (REXS) experiments have confirmed the A-type AFM order in EuCd_2As_2 [4]. Here, we investigate the magnetic structure of EuZn_2As_2 .

There is a visible difference in the anisotropy of the magnetic susceptibility between EuZn_2As_2 and EuCd_2As_2 . Figures 2(a) and 2(b) show that the ratio χ_{ab}/χ_c is near one in EuZn_2As_2 and near four in EuCd_2As_2 . Figures 2(c) and 2(d) show that the ratio of saturation fields with $(H\parallel c)/(H\parallel ab)$ is $(3.6 \text{ T})/(2.5 \text{ T}) = 1.4$ in EuZn_2As_2 versus $(1.8 \text{ T})/(0.8 \text{ T}) = 2.2$ in EuCd_2As_2 . These observations can be interpreted in two

ways. Either, the magnetic ordering in EuZn_2As_2 is C type unlike A type in EuCd_2As_2 , or it is A type but with smaller anisotropy. We will show the latter to be correct using neutron scattering and first-principle calculations.

The smaller magnetic anisotropy of EuZn_2As_2 compared to EuCd_2As_2 is also reflected in the resistivity data in Figs. 2(e) and 2(f). The zero-field resistivity of EuZn_2As_2 is isotropic [Fig. 2(e)] whether the electric current is applied out-of-plane ($J\parallel c \rightarrow \rho_c$) or in-plane ($J\parallel ab \rightarrow \rho_{ab}$). In contrast, the resistivity of EuCd_2As_2 is anisotropic with $\rho_c/\rho_{ab} \approx 5$ from room to low temperatures [Fig. 2(f)] [1]. In both cases, $\rho(T)$ shows a peak near T_N as it increases in the region of magnetic fluctuations $T_N < T < 3T_N$ and decreases at $T < T_N$. Also, in both cases, the room temperature resistivity is more than 20 m Ω cm, which is 20 times larger than the localization (Ioffe-Regel) limit [29]. Nonetheless, $\rho(T)$ shows a mild decrease with temperature. This so-called bad metal behavior is observed in conductors with strong correlations and/or incoherent scattering due to spin fluctuations [30,31].

The observation of a FM Weiss temperature despite AFM ordering in both EuZn_2As_2 and EuCd_2As_2 suggests a competition between FM and AFM correlations. We used first-principles calculations to analyze the total energies of various magnetic structures. All combinations of in-plane versus out-of-plane spins, FM or type-A, -C, -G AFM, and two types of 120 $^\circ$ rotational cells were considered. Details of these calculations can be found in Sec. VI of SM [26] (see, also, references [32–34] therein). These calculations predict that both EuCd_2As_2 and EuZn_2As_2 have an A-type AFM ground-state (Fig. S6 within SM [26]), which for EuCd_2As_2 is consistent with REXS experiments. A striking observation from this analysis is the small energy differences between all magnetic configurations. In EuZn_2As_2 , the largest energy difference is about 5 meV between the G-type and A-type AFM states with the latter being the ground state. In EuCd_2As_2 , the energy difference is even smaller, approximately 2 meV between the G-type and A-type AFM states. Such small energy differences approach the computational resolution, i.e., both C-type and A-type AFM states could be the ground state of either compound. The experimental implication is that the magnetic ground state of these materials can be easily manipulated by external pressure or strain, which creates an exciting platform for tuning a topological band structure by tuning the magnetic structure [6].

C. Neutron Diffraction

Neutron diffraction can unambiguously distinguish between the A- and C-type magnetic ordering in EuZn_2As_2 . The magnetic Bragg peaks (\vec{Q}_{mag}) of the A- and C-type orders are respectively indexed by $\vec{k} = (0, 0, 1/2)$ and $(1/2, 0, 0)$ ordering vectors ($\vec{Q}_{\text{mag}} = \vec{Q}_{\text{nuc}} \pm \vec{k}$ where \vec{Q}_{nuc} is the position of a nuclear Bragg peak). Thus, we collected neutron diffraction scans along the (H00) and (00L) directions within the first Brillouin zone of various nuclear zone centers at 1.5 K, well below $T_N = 19.6$ K. Eleven Bragg peaks were found that could be indexed by a $\vec{k} = (0, 0, 1/2)$ ordering vector [see rocking scans for $\vec{Q} = (0, 0, 3/2)$ plotted in Fig. 3(a) as an example], while no $\vec{k} = (1/2, 0, 0)$ Bragg peaks were observed.

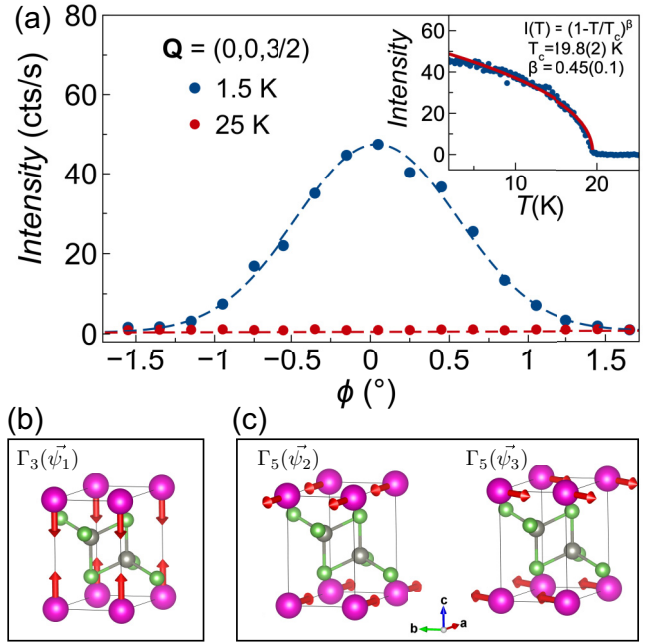


FIG. 3. (a) Rocking scan measured at $\vec{Q} = (0, 0, 3/2)$ and collected for both $T = 25$ K and $T = 1.5$ K. The top right inset shows the order parameter measurement, which was also acquired at $\vec{Q} = (0, 0, 3/2)$. The real part of the basis vectors resulting from the representation symmetry analysis of space group 164 with a $\vec{k} = (0, 0, 1/2)$ ordering vector is presented in (b) and (c). Panel (c) shows the $\vec{\psi}_1$ ($\vec{\psi}_2$ and $\vec{\psi}_3$) basis vector(s) corresponding to the Γ_3 (Γ_5) manifold where strictly out-of-plane (in-plane) spin component is allowed. Eu, Zn, As atoms are shown as magenta, green, gray balls, respectively.

Also, no $\vec{k} = (0, 0, 0)$ peaks were observed, ruling out FM configurations consistent with the absence of $M(H)$ hysteresis in Fig. 2(c). Thus, neutron scattering confirms A-type AFM order predicted by DFT.

Note that within the A-type order, symmetry analysis tells us that the spins can point either out-of-plane or in-plane [Figs. 3(b) and 3(c)], corresponding to two different irreducible representations, Γ_3 and Γ_5 . Γ_3 has a single basis vector ($\vec{\psi}_1$) with strictly out-of-plane spins [Fig. 3(b)]. Γ_5 has two basis vectors ($\vec{\psi}_2$ and $\vec{\psi}_3$) whose spin components are perpendicular to each other and are strictly pointing within the ab plane [Fig. 3(c)]. The observation of magnetic Bragg peak at $\vec{Q} = (0, 0, L/2)$ positions [e.g., $\vec{Q} = (0, 0, 3/2)$ in Fig. 3] rules out the Γ_3 manifold because neutron scattering is only sensitive to magnetization perpendicular to the momentum transfer \vec{Q} .

The inset of Fig. 3(a) shows that the order parameter [intensity of the $\vec{Q} = (0, 0, 3/2)$ peak] approaches the critical point continuously with an exponent $\beta = 0.45(0.1)$ close to the mean-field value $\beta = 0.5$. Thus, the AFM transition in EuZn_2As_2 is a second-order phase transition, described by a single irreducible representation Γ_5 . Due to averaging over symmetrically related magnetic domains, neutron diffraction cannot distinguish between ψ_2 and ψ_3 basis vectors. Also, an accurate estimate of the Eu^{2+} moment size is not possible due to high absorption cross section of the Eu^{2+} ions.

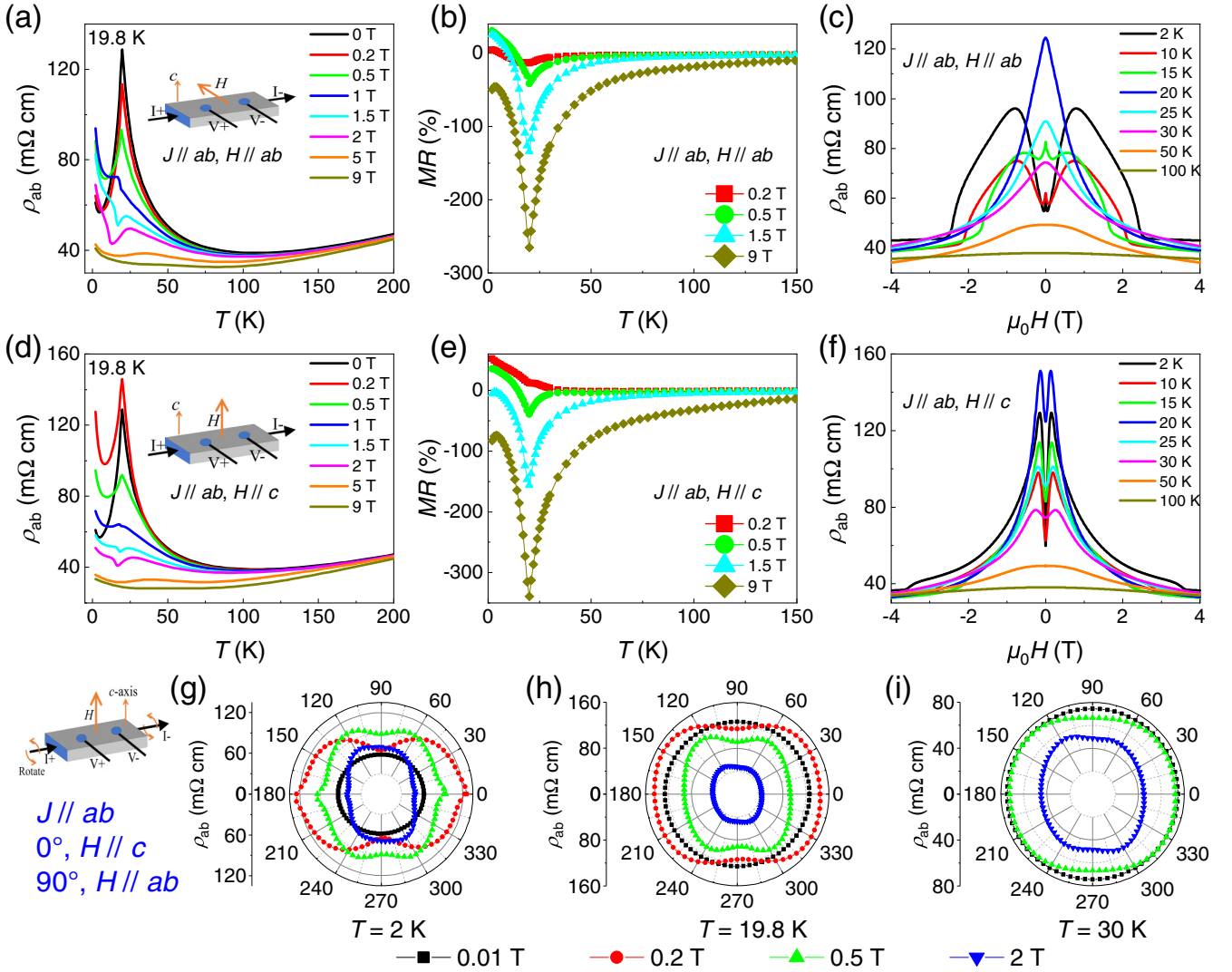


FIG. 4. (a) Temperature dependence of in-plane resistivity with fields along ab -plane. (b) Magnetoresistance with in-plane fields as a function of temperature. (c) Field dependence of in-plane resistivity at several temperatures. [(d), (e), (f)] $\rho_{ab}(T)$, $MR(T)$, and $\rho_{ab}(H)$ with out-of-plane fields, respectively. [(g), (h), (i)] Angle dependence of in-plane resistivity under several fields at 2 K, 19.8 K, and 30 K, respectively.

D. Magnetoresistance

The temperature, field, and angle dependence of in-plane resistivity (ρ_{ab}) are summarized in Fig. 4. Given the isotropic behavior of EuZn_2As_2 (Fig. 2), the data for ρ_c are similar to ρ_{ab} as seen in Fig. S4 within SM [26]. The data collected with in-plane field ($H \parallel ab$) are presented in Figs. 4(a), 4(b), and 4(c) while Figs. 4(d), 4(e), and 4(f) show the data with out-of-plane field ($H \parallel c$). In either direction, the resistivity of EuZn_2As_2 shows a negative magnetoresistance (MR) near T_N and a positive MR at small fields. The two effects are discussed separately below.

(a) *Negative MR near T_N .* As discussed earlier, the zero-field resistivity of EuZn_2As_2 shows a peak near T_N [Fig. 2(e)]. This peak is rapidly suppressed when a magnetic field is applied in either $H \parallel ab$ or $H \parallel c$ direction [Figs. 4(a) and 4(d)]. We define magnetoresistance as $MR = 100\% \times (\rho(H) - \rho(0))/\rho(H)$ and plot it as a function of temperature at several fields in Figs. 4(b) and 4(e). The negative MR begins from high temperature (> 100 K), reaches a maximum of -340%

at T_N under a 9 T field, and drops to about -100% below T_N giving rise to the peak near T_N [Figs. 4(b) and 4(e)]. A similar effect has recently been reported in EuCd_2P_2 (isostructural to EuZn_2As_2) but with two differences: (i) the negative MR is approximately 20 times larger for in-plane current (ρ_{ab}) in EuCd_2P_2 and (ii) it shows a tenfold anisotropy between out-of-plane and in-plane current directions ($\rho_c/\rho_{ab} = 10$) unlike the isotropic behavior of EuZn_2As_2 (Fig. S4 within SM [26]). It has been argued that the negative MR in EuCd_2P_2 is due to magnetic fluctuations in the region $T_N < T < 3T_N$ [31]. Within the spin fluctuation mechanism, the smaller magnitude of MR in EuZn_2As_2 could be related to the smaller magnetic anisotropy compared to EuCd_2P_2 . A higher in-plane anisotropy leads to stronger spin fluctuations, higher scattering rate, and larger MR.

(b) *Positive MR at small fields.* In addition to the negative MR, a positive MR is also observed in EuZn_2As_2 at low temperatures and under small fields. For $H \parallel ab$ and $T = 2$ K [the black curve in Fig. 4(c)] ρ_{ab} increases with increasing

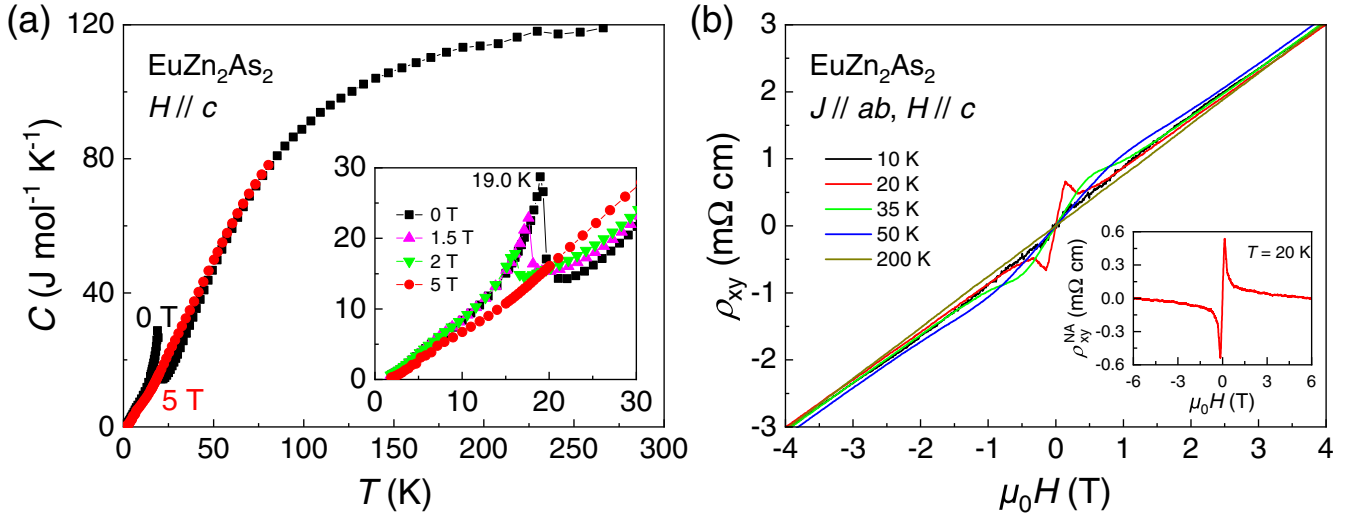


FIG. 5. (a) Temperature dependence of heat capacity for EuZn_2As_2 at several fields. (b) Magnetic field dependence of the Hall resistivity at various temperatures. The fields are along crystallographic c axis while the current is in ab plane.

field initially, and the positive MR is about 40% at $H = 0.8$ T. For $\rho_{ab}(H_{ab})$ curves [Fig. 4(c)], the positive MR gradually vanishes as the temperature approaches $T_N = 19.6$ K. In contrast, for $\rho_{ab}(H_c)$ curves, the positive MR survives up to 30 K [Fig. 4(f)]. The positive MR for $\rho_{ab}(H_c)$ shows a peak at about 0.15 T at all temperatures before it turns into a negative MR. It is worth noting that the magnitude of positive MR at 2 K with $H \parallel c$ is 52% ($\Delta\rho/\rho(0) = 107\%$), i.e., ρ_{ab} doubles in a field as small as 0.15 T.

Note that the positive MR depends on the field direction and arises only when the temperature is close to or lower than T_N . Therefore, it may be related to the close competition between different magnetic structures in EuZn_2As_2 shown by our DFT calculations (Fig. S6 within SM [26]). The external magnetic field can disturb the balance between competing AFM states (A-type and C-type) and lead to short-range AFM fluctuations that enhance electronic scattering and lead to the positive MR. A similar mechanism has been proposed in thin film AFM oxides [35].

Figures 4(g), 4(h), and 4(i) show 360° scans of the resistivity at 2 K, 19.8 K (T_N), and 30 K, respectively. The magnitude of the resistivity shows a weak dependence on the field direction near and above T_N consistent with nearly isotropic magnetization in Fig. 2. However, well below T_N at 2 K, Fig. 4(g) shows a twofold anisotropy in ρ_{ab} at $H = 0.2$ T (red circles). This observation is consistent with field-induced fluctuations between different magnetic states in EuZn_2As_2 .

E. Heat Capacity

Figure 5(a) shows the heat capacity of EuZn_2As_2 . The peak at 19.0 K is consistent with the AFM transition in $\rho(T)$ and $\chi(T)$ data in Fig. 2. As seen in the inset of Fig. 5(a), the heat capacity peak is suppressed by increasing the field from zero to 5 T. The parallel suppression of the magnetic entropy and resistivity with field shows that the negative magnetoresistance in EuZn_2As_2 is due to the suppression of spin scattering with increasing field.

F. Nonlinear Anomalous Hall Effect

The field dependence of the Hall resistivity for EuZn_2As_2 is shown in Fig. 5(b). The value of ρ_{xy} increases linearly with the field when the temperature is well above T_N , e.g., at $T = 200$ K in Fig. 5(b). From the positive slope of this ordinary Hall effect (OHE), the carriers are identified as hole type with the density $n = 8.6(2) \times 10^{17} \text{ cm}^{-3}$. The field dependence of ρ_{xy} becomes nonlinear as the temperature is decreased. The characteristic peak in the 20 K curve at 0.14 T in Fig. 5(b) is referred to as the nonlinear anomalous Hall effect (NLAHE) because it is not linear in either B or M . It is diminished rapidly below $T_N = 19.6$ K and vanishes below 10 K.

To analyze the NLAHE, the total Hall resistivity can be expressed as a sum of three contributions, $\rho_{xy} = R_0B + R_S M + \rho_{xy}^{\text{NA}}$, where R_0B is linear in B and represents the OHE, $R_S M$ is linear in M and represents the conventional anomalous Hall effect (AHE), and ρ_{xy}^{NA} is not linear in either B or M and represents the NLAHE [2]. The inset of Fig. 5(b) shows ρ_{xy}^{NA} as a function of field at 20 K after subtracting the OHE and AHE contributions (see also Fig. S5 within SM [26]). At the peak position, the NLAHE constitutes 83% of the total Hall resistivity ($\rho_{xy}^{\text{NA}}/\rho_{xy} = 0.83$) in EuZn_2As_2 . A similar behavior is observed in EuCd_2As_2 , where $\rho_{xy}^{\text{NA}}/\rho_{xy} = 0.97$ [2–4]. Both the sheer magnitude of ρ_{xy}^{NA} and the ratio $\rho_{xy}^{\text{NA}}/\rho_{xy}$ in EuX_2As_2 systems are larger than in materials with a helical magnetic order such as MnSi, MnGe, Fe_5Sn_3 , and Mn_2CoAl [36–39], and in materials with a large intrinsic (Berry phase) nonlinear AHE such as the half-Heusler compounds GdPtBi and DyPtBi [40,41].

G. Electronic Structure

To investigate the underlying differences between EuZn_2As_2 and EuCd_2As_2 , we calculated their band structures assuming type-A AFM order and in-plane spins consistent with experimental findings. The most significant difference in the electronic structures [Figs. 6(a) and 6(b)] is in the band just

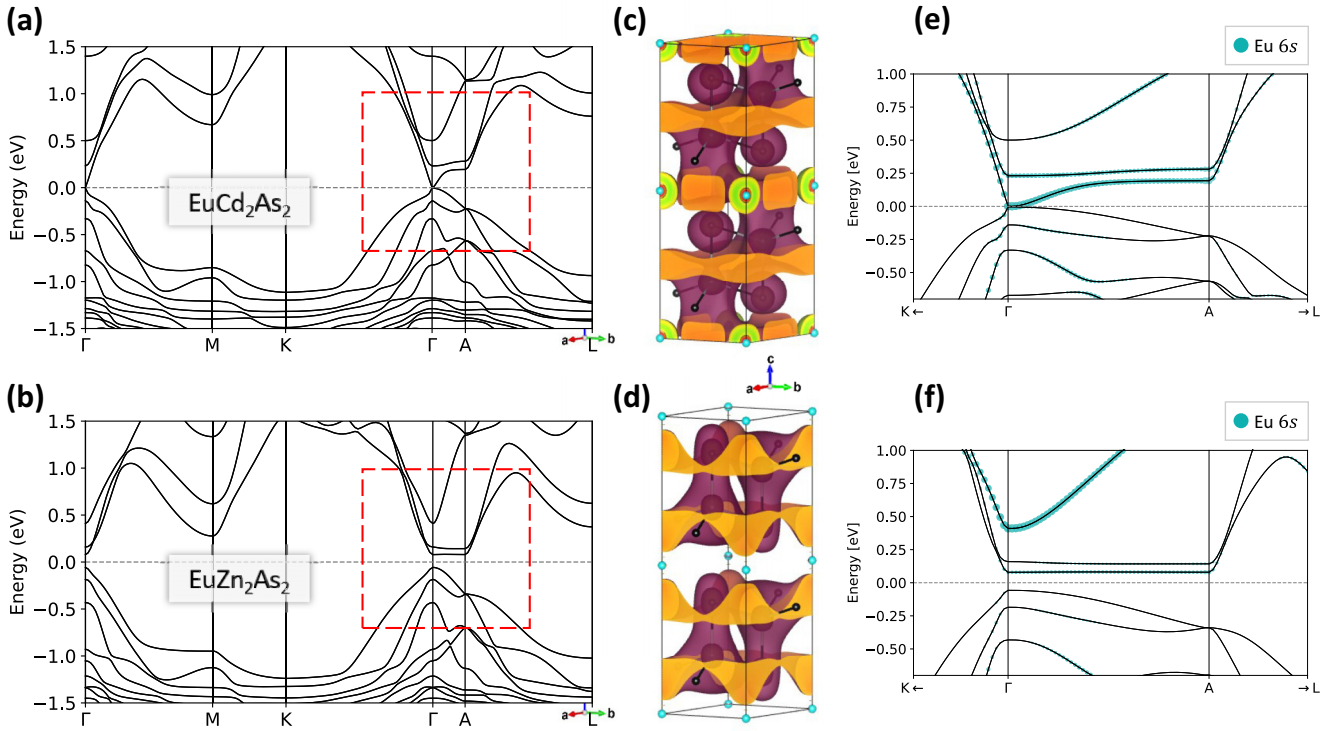


FIG. 6. [(a), (b)] Band structures of EuCd_2As_2 and EuZn_2As_2 . The red, dashed box indicates the zoomed-in region in subfigures (e) and (f). [(c), (d)] Charge densities (purple surface) in EuCd_2As_2 and EuZn_2As_2 for the conduction band at the Γ -point. Eu, Zn, As atoms are shown as cyan, brown, black balls, respectively. [(e), (f)] Band projections onto the Eu-6s orbitals in EuCd_2As_2 and EuZn_2As_2 .

above the Fermi energy along Γ -A, with EuCd_2As_2 showing much greater dispersion and a band touching at Γ , unlike the gapped and flatter bands in EuZn_2As_2 . Experimentally EuZn_2As_2 is not an insulator, so we expect some amount of disorder and doping to be present in the material.

In order to gain more insight into this interesting region of the band structure, the charge density of the first band above the Fermi level at the Γ point are plotted in Figs. 6(c) and 6(d) for both EuCd_2As_2 and EuZn_2As_2 at an isosurface threshold of 2×10^{-3} electrons. Qualitatively, the frontier orbitals of EuCd_2As_2 exhibit an antibonding character within the CdAs_4 layer, unlike the bonding character within the ZnAs_4 layer in EuZn_2As_2 . Another notable difference between the two is the charge density of Eu, being significant in EuCd_2As_2 but almost negligible in EuZn_2As_2 .

To better understand the nature of the Eu atom electron density, the projections of Eu-6s orbitals onto the bands are shown in Figs. 6(e) and 6(f) for the region indicated by the dashed red squares in Figs. 6(a) and 6(b). Even though the overall orbital character of the conduction band is Cd-5s and Zn-4s, respectively (see Figs. S9 and S10 within in SM [26]), the Eu-6s character provides unique insights. The band that is predominantly Eu-6s is different between EuCd_2As_2 and EuZn_2As_2 , the former being the first band above the Fermi level, and the latter being the third band. Along with the differences in the Cd(Zn) $4(3)d_{z^2}$ and As $4p_z$ orbital projections onto the band structures (see Fig. S10 within SM [26]), the implication is that the third band above the Fermi energy in

EuZn_2As_2 gets pushed down through the two lower bands to become the first band above the Fermi energy in EuCd_2As_2 .

Considering the dispersion of EuCd_2As_2 near Γ can help to explain the transport and magnetic anisotropy seen in Sec. III B. As can most clearly be seen in the first band above the Fermi level in panel (e) the effective electron mass is small along K - Γ , corresponding to the ab -plane direction, compared to the effective mass along Γ -A, corresponding to the c -axis direction. This difference in effective electron mass could lead to the anisotropy seen in the experiments.

The origin of the isotropic magnetic and transport measurements in EuZn_2As_2 is not as clear-cut. Since the first-principles calculations predict EuZn_2As_2 to be an insulator, the origin is still an open question although we hypothesize that it is related to a 3-dimensional disorder in the material. Eu can exist in a multivalent state of $2+$ and $3+$, and given the stoichiometry of these compounds, both valence states of Eu likely exist in each material. In EuCd_2As_2 because of the extended nature of the $4d$ orbitals in Cd, it is likely that the molecular-like orbital formed by Eu and Cd hybridization is more uniform across the material. However, the $3d$ orbitals of Zn are less extended so cannot smooth the mixture of $2+$ and $3+$ Eu, leading to 3-dimensional disorder in EuZn_2As_2 which would mask any underlying anisotropy. A method to test this hypothesis, which is left to future work, is to measure the L edge of Eu with x-ray absorption spectroscopy (XAS) to determine if the samples of EuZn_2As_2 contain a mixture of $2+$ and $3+$ Eu, leading to 3D disorder.

IV. CONCLUSIONS

The comparative study presented here between EuZn_2As_2 and EuCd_2As_2 can be summarized as follows. Both compounds are semimetals with a small concentration of hole carriers ($10^{17-18} \text{ cm}^{-3}$), hence the large OHE. Both compounds have A-type AFM order and exhibit a parallel suppression of the magnetic entropy and resistivity with field. Thus, the negative MR is likely a result of suppressing the spin fluctuations with increasing field. The main differences between the two compounds is in their respective T_N values and the anisotropy of both magnetic susceptibility and magnetoresistance. Whereas χ_c and ρ_c are 4–5 times larger than χ_{ab} and ρ_{ab} in EuCd_2As_2 ($T_N = 9.2 \text{ K}$), they are comparable in EuZn_2As_2 ($T_N = 19.6 \text{ K}$).

What underlies this anisotropy difference between EuZn_2As_2 and EuCd_2As_2 ? We can eliminate a structural origin since the two materials have nearly the same c/a ratios, and we can eliminate a magnetic origin since both materials have been shown to have type-A AFM order, leaving the origin to likely be electronic. Indeed, when comparing the electronic structures from first-principles calculations, there are significant differences between the two materials in their first few bands above the Fermi level. The first band above the Fermi level in EuCd_2As_2 shows high dispersion and a band touching point at Γ , has 3D charge density at that point, and it has significant Eu 6s character. In contrast, DFT predicts EuZn_2As_2 to be gapped with a flat band above the Fermi energy, that band's charge density at Γ is in separated 2D planes, and the third band above the Fermi energy

shows the most significant Eu 6s character. The charge and magnetization anisotropy of EuCd_2As_2 is likely due to the difference in effective mass of the first band above the Fermi level, which shows very different dispersion in the ab plane versus along the c axis. The lack of anisotropy in EuZn_2As_2 is still an open question but is likely due to a 3D disorder of Eu valence states which cannot be smoothed by the d orbitals of Zn because they are less extended than those of Cd.

Studying EuZn_2As_2 as an analog to EuCd_2As_2 has helped elucidate the effect of tuning between $X = \text{Cd}, \text{Zn}$ on the temperatures of resistivity peak and NLAHE, and on the anisotropy of magnetization and transport.

ACKNOWLEDGMENTS

This material is based upon work supported by the Air Force Office of Scientific Research under Award No. FA2386-21-1-4059. The work at Stanford University and SLAC National Accelerator Laboratory was supported by the U.S. Department of Energy, Office of Basic Energy Sciences, Division of Materials Sciences and Engineering, under Contract No. DE-AC02-76SF00515, for theoretical analysis and calculations. This research used resources of the National Energy Research Scientific Computing Center (NERSC), a U.S. Department of Energy Office of Science User Facility, operated under Contract No. DEAC02-05CH11231. Any mention of commercial products is intended solely for fully detailing experiments; it does not imply recommendation or endorsement by NIST.

-
- [1] H. P. Wang, D. S. Wu, Y. G. Shi, and N. L. Wang, Anisotropic transport and optical spectroscopy study on antiferromagnetic triangular lattice EuCd_2As_2 : An interplay between magnetism and charge transport properties, *Phys. Rev. B* **94**, 045112 (2016).
- [2] X. Cao, J.-X. Yu, P. Leng, C. Yi, Y. Yang, S. Liu, L. Kong, Z. Li, X. Dong, Y. Shi, J. Zang, and F. Xiu, Giant nonlinear anomalous hall effect induced by spin-dependent band structure evolution, [arXiv:2103.09395](https://arxiv.org/abs/2103.09395).
- [3] J.-Z. Ma, S. M. Nie, C. J. Yi, J. Jandke, T. Shang, M. Y. Yao, M. Naamneh, L. Q. Yan, Y. Sun, A. Chikina *et al.*, Spin fluctuation induced Weyl semimetal state in the paramagnetic phase of EuCd_2As_2 , *Sci. Adv.* **5**, eaaw4718 (2019).
- [4] M. C. Rahn, J.-R. Soh, S. Francoual, L. S. I. Veiga, J. Stremper, J. Mardegan, D. Y. Yan, Y. F. Guo, Y. G. Shi, and A. T. Boothroyd, Coupling of magnetic order and charge transport in the candidate dirac semimetal EuCd_2As_2 , *Phys. Rev. B* **97**, 214422 (2018).
- [5] J.-R. Soh, F. de Juan, M. G. Vergniory, N. B. M. Schröter, M. C. Rahn, D. Y. Yan, J. Jiang, M. Bristow, P. Reiss, J. N. Blandy, Y. F. Guo, Y. G. Shi, T. K. Kim, A. McCollam, S. H. Simon, Y. Chen, A. I. Coldea, and A. T. Boothroyd, Ideal Weyl semimetal induced by magnetic exchange, *Phys. Rev. B* **100**, 201102(R) (2019).
- [6] L.-L. Wang, N. H. Jo, B. Kuthanazhi, Y. Wu, R. J. McQueeney, A. Kaminski, and P. C. Canfield, Single pair of Weyl fermions in the half-metallic semimetal EuCd_2As_2 , *Phys. Rev. B* **99**, 245147 (2019).
- [7] J. Ma, H. Wang, S. Nie, C. Yi, Y. Xu, H. Li, J. Jandke, W. Wulfhchel, Y. Huang, D. West *et al.*, Emergence of nontrivial low-energy dirac fermions in antiferromagnetic EuCd_2As_2 , *Adv. Mater.* **32**, 1907565 (2020).
- [8] J.-R. Soh, E. Schierle, D. Y. Yan, H. Su, D. Prabhakaran, E. Weschke, Y. F. Guo, Y. G. Shi, and A. T. Boothroyd, Resonant x-ray scattering study of diffuse magnetic scattering from the topological semimetals EuCd_2As_2 and EuCd_2Sb_2 , *Phys. Rev. B* **102**, 014408 (2020).
- [9] P. Schiffer, A. P. Ramirez, W. Bao, and S.-W. Cheong, Low Temperature Magnetoresistance and the Magnetic Phase Diagram of $\text{La}_{1-x}\text{Ca}_x\text{MnO}_3$, *Phys. Rev. Lett.* **75**, 3336 (1995).
- [10] M. A. Subramanian, B. H. Toby, A. P. Ramirez, W. J. Marshall, A. W. Sleight, and G. H. Kwei, Colossal magnetoresistance without $\text{Mn}^{3+}/\text{Mn}^{4+}$ double exchange in the stoichiometric pyrochlore $\text{Tl}_2\text{Mn}_2\text{O}_7$, *Science* **273**, 81 (1996).
- [11] A. Ramirez, R. J. Cava, and J. Krajewski, Colossal magnetoresistance in Cr-based chalcogenide spinels, *Nature (London)* **386**, 156 (1997).
- [12] J. Y. Chan, S. M. Kauzlarich, P. Klavins, R. N. Shelton, and D. J. Webb, Colossal magnetoresistance in the transition-metal Zintl compound $\text{Eu}_{14}\text{MnSb}_{11}$, *Chem. Mater.* **9**, 3132 (1997).
- [13] I. R. Fisher, T. A. Wiener, S. L. Bud'ko, P. C. Canfield, J. Y. Chan, and S. M. Kauzlarich, Thermodynamic and transport

- properties of single-crystal $\text{Yb}_{14}\text{MnSb}_{11}$, *Phys. Rev. B* **59**, 13829 (1999).
- [14] J. Jiang and S. M. Kauzlarich, Colossal magnetoresistance in a rare earth Zintl compound with a new structure type: EuIn_2P_2 , *Chem. Mater.* **18**, 435 (2006).
- [15] A. M. Goforth, P. Klavins, J. C. Fettinger, and S. M. Kauzlarich, Magnetic properties and negative colossal magnetoresistance of the rare earth Zintl phase EuIn_2As_2 , *Inorg. Chem.* **47**, 11048 (2008).
- [16] J. Rodríguez-Carvajal, Recent advances in magnetic structure determination by neutron powder diffraction, *Phys. B: Condens. Matter* **192**, 55 (1993).
- [17] A. Wills, A new protocol for the determination of magnetic structures using simulated annealing and representational analysis (SARA/h), *Phys. B: Condens. Matter* **276-278**, 680 (2000).
- [18] G. Kresse and D. Joubert, From ultrasoft pseudopotentials to the projector augmented-wave method, *Phys. Rev. B* **59**, 1758 (1999).
- [19] J. P. Perdew, K. Burke, and M. Ernzerhof, Generalized Gradient Approximation Made Simple, *Phys. Rev. Lett.* **77**, 3865 (1996).
- [20] G. Kresse and J. Furthmüller, Efficiency of *ab-initio* total energy calculations for metals and semiconductors using a plane-wave basis set, *Comput. Mater. Sci.* **6**, 15 (1996).
- [21] G. Kresse and J. Furthmüller, Efficient iterative schemes for *ab initio* total-energy calculations using a plane-wave basis set, *Phys. Rev. B* **54**, 11169 (1996).
- [22] G. Kresse and J. Hafner, *Ab initio* molecular dynamics for liquid metals, *Phys. Rev. B* **47**, 558 (1993).
- [23] G. Kresse and J. Hafner, *Ab initio* molecular-dynamics simulation of the liquid-metal–amorphous-semiconductor transition in germanium, *Phys. Rev. B* **49**, 14251 (1994).
- [24] Y. Xu, Z. Song, Z. Wang, H. Weng, and X. Dai, Higher-Order Topology of the Axion Insulator EuIn_2As_2 , *Phys. Rev. Lett.* **122**, 256402 (2019).
- [25] S. L. Dudarev, G. A. Botton, S. Y. Savrasov, C. J. Humphreys, and A. P. Sutton, Electron-energy-loss spectra and the structural stability of nickel oxide: An LSDA+U study, *Phys. Rev. B* **57**, 1505 (1998).
- [26] See Supplemental Material at <http://link.aps.org/supplemental/10.1103/PhysRevB.105.165122> for complementary experimental data and details about first-principle calculations.
- [27] J. O. Dimmock and A. J. Freeman, Band Structure and Magnetism of Gadolinium Metal, *Phys. Rev. Lett.* **13**, 750 (1964).
- [28] D. Li, J. Pearson, S. D. Bader, D. N. McIlroy, C. Waldfried, and P. A. Dowben, Spin-polarized photoemission studies of the exchange splitting of the Gd *5d* electrons near the curie temperature, *Phys. Rev. B* **51**, 13895 (1995).
- [29] A. F. Ioffe and A. R. Regel, Non-crystalline, amorphous, and liquid electronic semiconductors, *Prog. Semicond.* **4**, 237 (1960).
- [30] V. J. Emery and S. A. Kivelson, Superconductivity in Bad Metals, *Phys. Rev. Lett.* **74**, 3253 (1995).
- [31] Z.-C. Wang, J. D. Rogers, X. Yao, R. Nichols, K. Atay, B. Xu, J. Franklin, I. Sochnikov, P. J. Ryan, D. Haskel, and F. Tafti, Colossal magnetoresistance without mixed valence in a layered phosphide crystal, *Adv. Mater.* **33**, 2005755 (2021).
- [32] X. Wang, W. Li, C. Wang, J. Li, X. Zhang, B. Zhou, Y. Chen, and Y. Pei, Single parabolic band transport in p-type EuZn_2Sb_2 thermoelectrics, *J. Mater. Chem. A* **5**, 24185 (2017).
- [33] J. Sun, R. C. Remsing, Y. Zhang, Z. Sun, A. Ruzsinszky, H. Peng, Z. Yang, A. Paul, U. Waghmare, X. Wu *et al.*, Accurate first-principles structures and energies of diversely bonded systems from an efficient density functional, *Nat. Chem.* **8**, 831 (2016).
- [34] J. Sun, A. Ruzsinszky, and J. P. Perdew, Strongly Constrained and Appropriately Normed Semilocal Density Functional, *Phys. Rev. Lett.* **115**, 036402 (2015).
- [35] J. Zhang, W.-J. Ji, J. Xu, X.-Y. Geng, J. Zhou, Z.-B. Gu, S.-H. Yao, and S.-T. Zhang, Giant positive magnetoresistance in half-metallic double-perovskite Sr_2CrWO_6 thin films, *Sci. Adv.* **3**, e1701473 (2017).
- [36] A. Neubauer, C. Pfleiderer, B. Binz, A. Rosch, R. Ritz, P. G. Niklowitz, and P. Böni, Topological Hall Effect in the A Phase of MnSi , *Phys. Rev. Lett.* **102**, 186602 (2009).
- [37] N. Kanazawa, Y. Onose, T. Arima, D. Okuyama, K. Ohoyama, S. Wakimoto, K. Kakurai, S. Ishiwata, and Y. Tokura, Large Topological Hall Effect in a Short-Period Helimagnet MnGe , *Phys. Rev. Lett.* **106**, 156603 (2011).
- [38] H. Li, B. Ding, J. Chen, Z. Li, E. Liu, X. Xi, G. Wu, and W. Wang, Large anisotropic topological Hall effect in a hexagonal non-collinear magnet Fe_5Sn_3 , *Appl. Phys. Lett.* **116**, 182405 (2020).
- [39] B. M. Ludbrook, G. Dubuis, A.-H. Puichaud, B. J. Ruck, and S. Granville, Nucleation and annihilation of skyrmions in Mn_2CoAl observed through the topological Hall effect, *Sci. Rep.* **7**, 13620 (2017).
- [40] H. Zhang, Y. L. Zhu, Y. Qiu, W. Tian, H. B. Cao, Z. Q. Mao, and X. Ke, Field-induced magnetic phase transitions and the resultant giant anomalous Hall effect in the antiferromagnetic half-Heusler compound DyPtBi , *Phys. Rev. B* **102**, 094424 (2020).
- [41] T. Suzuki, R. Chisnell, A. Devarakonda, Y.-T. Liu, W. Feng, D. Xiao, J. W. Lynn, and J. G. Checkelsky, Large anomalous Hall effect in a half-Heusler antiferromagnet, *Nat. Phys.* **12**, 1119 (2016).